A novel vortex-based velocity sampling method for the actuator-line modeling of floating offshore wind turbines in windmill state

Andrea G. Sanvito [a], Agnese Firpo [a], Paolo Schito [b], Vincenzo Dossena [a], Alberto Zasso [b], Giacomo Persico [a],*

[a] *Department of Energy, Politecnico di Milano, Via Lambruschini 4, Milano, 20156, Italy*
[b] *Department of Mechanical Engineering, Politecnico di Milano, Via La Masa 1, Milano, 20156, Italy*

A R T I C L E   I N F O

A B S T R A C T

The fluid-dynamic simulation of wind turbine aerodynamics is typically tackled by applying multi-fidelity computational tools. In this context, the so-called actuator line model combines a low-fidelity treatment of the rotor with a high-fidelity resolution of the wake. In this paper, a novel formulation of the actuator line model proposes a vortex-based method to sample the flow around the rotor to rigorously assign the forces imparted by the blades. This new technique is implemented into an in-house code developed within the OpenFOAM environment, and it is validated against wind-tunnel experiments on a laboratory-scale horizontal-axis wind turbine operated in fixed-bottom and floating conditions. The calculations are also compared against multi-fidelity simulations performed, on the same test case, in the frame of the OC6 Phase III project. The simulation results, obtained after a systematic analysis and selection of the model parameters, exhibit a remarkable agreement with the available experiments and place the present code in the proper ranking of fidelity levels, in-between momentum-balance methods and blade-resolved CFD models. Finally, the calculations for surge and pitch platform motions demonstrate the capability of the proposed technique to reliably predict the aerodynamics of turbine rotors in dynamic operation at affordable computational cost.

1. Introduction

In recent years, there has been a growing interest in deploying offshore wind turbines to exploit the potential of stronger and more uniform winds in off-coast deep see, where floating foundations have to be adopted. The challenges in designing Floating Offshore Wind Turbines (FOWTs) entails a holistic approach including hydrodynamics, aerodynamics and structural integrity aspects, as well as in the control of the entire floating wind farm and its maintenance.

The extremely large scale of the machines involved in the technology makes unfeasible real-scale experiments and, hence, the design and analysis of floating wind farms almost entirely rely on computational tools. However, the cost and difficulty of simulation models which fully resolve the flow around the rotor and in the wake, based on Computational Fluid Dynamics (CFD), has historically prevented from a systematic use of such fully-resolved models in wind turbine technology, and prompted researchers to develop simulation tools in a wide range of fidelity – and computational cost – level [1]. For wind turbine design, the research focused on low-fidelity models, i.e., models based on the Blade Element Momentum (BEM) theory or on the Lifting Line

Free-Vortex Wake (LLFVW) approach, which benefit from a very low simulation cost but demand for a wide validation (with experiments and higher-fidelity codes). For wind-farm design and control, instead, intermediate-fidelity models combining the BEM theory at the rotor level with CFD were found to provide both a reliable rotor aerodynamic prediction and a high resolution in the wake, while saving computational runtime with respect to the fully-resolved simulation tools.

In this paper, an intermediate-fidelity simulation tool based on the Actuator-Line Model (ALM) is presented and applied to simulate fixed-bottom and floating wind turbines. The ALM combines the advantages from low-fidelity (BEM, FVW) and high-fidelity (CFD) tools: the rotor aerodynamics is modeled with BEM theory, by replacing the blades with aerodynamic forces, evaluated by resorting to look-up tables, applied in the actuator line (AL) point, and distributed in the numerical domain according to a specified spreading function; the wake resolution is inherited by a standard CFD approach which solves Navier–Stokes equation in the fluid domain. The main advantage of ALM lies in its

---

capability to achieve high resolution in the wake region, making it particularly suited to the study of wake-structure interactions, especially in floating wind farms. Moreover, by eliminating the resolution of the flow around each individual blade, the ALM guarantees a much reduced computational cost, compared to fully-resolved (or blade-resolved) CFD analyses.

The ALM, since its first formulation proposed in [2], poses a difficulty on the determination of the velocity vector of the free-stream at the blades from the distributed flow field calculated by the CFD simulation. This is crucial for the model, since the aerodynamic forces are evaluated by this velocity. However, the aerodynamic forces (the lift in particular) induce a perturbation, namely a local induction, in the region where the forces are distributed, associated to the onset of a bound vortex around the airfoil. According to the theory of rotational inviscid flows, the velocity sampled in the point of application of the forces (actuator point) [3], or in the center of pressure of the airfoil, should be free from the local induction of the bound vortex. Nevertheless, the numerical discretization may induce an error in this evaluation due to the inevitable interpolation in a region of severe velocity gradients, affecting the sampling result which is extremely sensitive to the location of the velocity sampling.

For this reason, several researchers proposed alternative strategies to account for the specific induction velocities originated by the Gaussian force distribution. Meyer Forsting et al. [4] corrected the induction accounting for the inviscid bound and trailing vortex. Churchfield et al. [5] proposed to use the force spreading function to weight the velocity in the sampling procedure, to eliminate the induction effect. Martínez-Tossas et al. [6] deviates from the hypothesis of inviscid vortex core, introducing the correction added by the drag force to the flow field. Lu and Portè-Agel [7] studied wind turbines in stable Atmospheric Boundary Layer (ABL) with LES; the determination of the inflow velocity and angles of attack is performed according to iterative procedures based on the engineering methods to subtract the effect of the bound vortex to the velocity field [8,9]. Arabgolarcheh et al. [10] applied the ALM to FOWTs where the definition of the velocity vector experienced by each blade station is determined by the accurate estimation of the inflow velocity, which encompasses the floating motion of the platform. In the same study, the velocities at each AL point are achieved with the method proposed by Jost et al. [11] named as Line Average technique. A similar approach, based on the sampling along the closed symmetric path to balance the induction given by the bound vortex, has been adopted by Melani et al. [12] for VAWTs.

The paper presents the comparison of three methods which share the feature of sampling velocity components from the CFD flow field following different strategies: (i) the line method averages velocities over upstream and downstream lines with respect to the AL point; (ii) the line average technique [11]; (iii) a novel vortex-based method which analytically calculates and subtracts the induction caused by the force kernel. The comparison aims at shedding light on the contribution of the bound vorticity, formulating a robust algorithm to extract angles of attack in ALMs simplifying the induction field as it was created by a concentrated bound vortex pursuing a physics–based approach. This method was applied to a wind turbine model operated in fixed-bottom conditions and in surge and pitch floating motion, and compared with experiments [13] and simulations performed with alternative computational techniques [14], showing the validity of the proposed method for FOWT applications.

This paper is structured as follows. The paper outlines experimental case set-ups and the computational framework of ALM with emphasis on the velocity sampling methods. Results of the application of aforementioned techniques are firstly presented for the fixed-bottom case. A thorough verification is discussed through the comparison with OC6 Phase III data and engineering methods. Finally the application in FOWTs is examined in details showing flow patterns around the AL during surge motion. Conclusions are drawn in the final paragraph with key findings of the research on the novel velocity sampling methods.

Table 1
DTU-10 MW RWT turbine parameters.
Source: Taken from [14].

Parameter	UNAFLOW Experiment
Rotor diameter [m]	2.38132
Blade length [m]	1.10166
Hub diameter [m]	0.178
Rotor overhang [m]	0.09467
Tilt angle [°]	5
Tower to shaft distance [m]	0.03667
Tower length [m]	1.6057
Tower base offset [m]	0.450

2. Case study

In this work, the new model is applied to laboratory cases to carry out an experimental verification. Specifically, the experimental data is derived from the UNAFLOW test campaign [13,15] performed in the large-scale wind tunnel of the Politecnico di Milano. These experimental data have been recently used to perform a multi-fidelity model comparison in OC6 Phase III project (IEA Task 30) [14].

2.1. Experimental set-up

The examined turbine has a diameter of 2.38 m and represents a 1:75 scaled laboratory model of the DTU 10 MW machine [16], with a twist distribution and tapered chord variation; the tilt angle is set so that the rotor plane is normal to the incoming flow. The three blades of the rotor feature the same airfoil shape along the blade span, namely the SD7032 profile. The blade profile was tested in a dedicated experimental campaign described in [13], from which the tabulated aerodynamic coefficients were extracted in the Reynolds number range $50'000 - 200'000$. In this paper 'Exp' label refers to the original UNAFLOW measurements. Experimental set-up and outputs are thoroughly described in [17].

The wind tunnel has a test-section of $13.84\,\text{m} \times 3.84\,\text{m}$ and is 35 m long. The free-stream velocity is measured by a Pitot tube positioned 3 turbine diameters upstream of the rotor, with an inflow turbulence intensity below 2% and an air density $\rho = 1.177\,\text{kg/m}^3$ [15]. The wind tunnel outlet is placed 7 m downstream of the wind turbine and the length of the tunnel upstream of the rotor was set so to let the wind tunnel boundary layer fully develop.

The experiments of the UNAFLOW test campaign were used, in this study, for the validation of fixed-bottom and floating turbine operation, this latter considering only surge platform motion.

Table 1 summarizes the key parameters for the set-up of experiments.

2.2. Load cases

In this paper multiple conditions, or load-cases (LC) in the following, are simulated to verify and validate the novel actuator line method for a wide range of turbine operation, namely for fixed-bottom installations as well as for floating ones, including both surge and pitch platform motions.

Fixed-bottom (LC1.1) and surge-platform (LC2.5) simulations were run in full coherence with the UNAFLOW experiments. These tests were performed with a rotor angular speed $\Omega = 240$ rpm in steady uniform wind with a free-stream velocity $U_0 = 4$ m/s, to simulate rated conditions at tip speed ratio $TSR = \frac{\Omega R}{U_0} = 7.5$. Beside the experimental validation, this paper also proposes a comparison against a selection of the computational results of OC6 Phase III participants. The pitch-platform (LC3.5) simulations were conceived to correspond to the surge ones, by keeping constant, beside wind velocity and rotor angular speed, the platform motion frequency and the rotor apparent wind (at the rotor hub). A selection of the computational results of OC6

Table 2
Surge and pitch load cases.

Load case	U_0 [m/s]	f [Hz]	A [m]/[°]	θ_{shift} [°]
LC1.1	4.0	–	–	–
LC2.5	4.0	1.0	0.035	7
LC3.5	4.0	1.0	1.400	7

Phase III participants will be used to assess the present pitch-platform simulations.

The time-dependent laws of surge displacement x and pitch angle θ_p are reported in Eqs. (1) and (2).

$$x(t) = A_s \sin\left(2\pi f_s t + \phi_s\right) \tag{1}$$

$$\theta_p(t) = A_p \sin\left(2\pi f_p t + \phi_p\right) \tag{2}$$

where $A_{s/p}$ is the motion amplitude and $f_{s/p}$ is the motion frequency. Subscripts s and p stand for surge or pitch respectively, and the motion lag is expressed by the phase shift ϕ. Leeward (namely, oriented along the incoming wind) displacement of the turbine is along the positive x-coordinate (i.e., from inlet to outlet of the tunnel, Fig. 3).

The velocity of the turbine due to floating motion is obtained with the first derivative of Eqs. (1) and (2).

A crucial parameter of floating turbine operation is the apparent wind perceived by the rotor due to the platform motion, defined as the relative wind speed perceived by the turbine. The minimum and maximum apparent wind velocities are found as $U_0 \pm 2\pi f_{s/p} A_{s/p}$ at the hub height. In LC2.5, the surge motion induces a velocity excursion of ± 0.22 m/s at hub height. As anticipated, the same excursion was imposed to the pitching motion of LC3.5. Surge LC2.5 and pitch LC3.5 cases are characterized by the same platform frequency, 1 Hz, see Table 2.

The considered surge and pitch load cases feature an unsteady coefficient k, defined as $k = \pi f_s c(r)/\sqrt{U_0^2 + (r\Omega)^2}$ according to [18], equal to 0.01 at 70% of the blade radius; this value is below the threshold beyond which airfoil unsteadiness may appear ($k = 0.05$). Besides, the rotor works in windmill state according to the definition of Kyle et al. [19], since the estimated effective induction factor a_s is equal to 0.35, well below the turbulent wake state limit of 0.5.

In the UNAFLOW experiments, the period of the surge motion started with the turbine in windward motion, corresponding to $\phi_s = 180°$ in Eq. (1). Moreover, at the starting phase of the period one blade was not perfectly vertical, but inclined by an angle of 7° with respect to the vertical direction. To fully match the conditions of the UNAFLOW experiments, LC2.5 simulations were performed setting the same phase and azimuthal shifts; for coherency with OC6 Phase III participants, LC3.5 simulations were performed with an azimuthal shift of 7°; the phase shift was, instead, set to zero (rotor pitching in the leeward direction at the beginning of the period).

3. Computational approach

3.1. Theoretical background of the actuator line model

The present in-house ALM algorithm is implemented in the CFD OpenFoam environment: the blades are represented as actuator lines interpolating a certain number of actuator points, in which the aerodynamic forces are applied. While the CFD solver provides the solution of the flow domain, the rotor aerodynamics is modeled with the BEM theory. The axial and tangential absolute velocity components (U_{ax} and U_{tg}) are obtained from the fluid domain by means of a velocity sampling technique; the magnitude (W in Eq. (3)) and direction of the relative velocity are essential for the ALM solution method, as they

influence the angle of attack (AoA) α, the Reynolds number Re, and the magnitude of the lift and drag forces L, D (Eq. (4)).

$$W = \sqrt{U_{ax}^2 + \left(\Omega r + U_{tg}\right)^2} \tag{3}$$

$$L = \frac{1}{2} C_L(\alpha, Re)\, W^2\, c \qquad D = \frac{1}{2} C_D(\alpha, Re)\, W^2\, c \tag{4}$$

where C_L and C_D are the lift and drag coefficients and c is the airfoil chord. The attack angle and Re number, in particular, are used to evaluate the aerodynamic coefficients from look-up tables provided as input to the ALM. In the present study, no dynamic corrections of the polars were applied. A preliminary analysis conducted in [14], indeed, showed that no hysteretic phenomenon should occur in the load conditions of interest. This is attributed to the angle of attack residing within the linear portion of the polar curves.

The point-wise forces are inserted and spread into the fluid domain according to a plane axisymmetric Gaussian kernel η_ϵ^{2D}, reported in Eq. (5), to distribute the force $\mathbf{f}$ over the cell centers, by means of a convolution (Eq. (6)):

$$\eta_\epsilon^{2D}(d) = \frac{1}{\epsilon^2 \pi} \exp\left[-\left(\frac{d}{\epsilon}\right)^2\right] \tag{5}$$

$$\mathbf{f}_\epsilon = \mathbf{f} \otimes \eta_\epsilon^{2D} \tag{6}$$

where d is the distance from the force center point and the characteristic scale ϵ of this so-called regularization kernel defines the semi-width of the force distribution region. The two-dimensional kernel expression originally reported in [3] is adopted here to circumvent the issue of numerical instabilities at the blade tip. In the physical 3D domain, the regularization kernel has a cylindrical shape, whose height is given by the distance between two adjacent mid-points of the segments delimited by actuator points.

Since ALM-CFD tool is capable to resolve the vortices shed by the blade tip, no correction at the blade end (e.g. Prandtl's tip loss model) is necessary to take account for the drag induced by the tip-vortex formation and mixing. However, the decrease of forces due to the equalization of the pressure between pressure and suction sides is not inherently reproduced in the ALM. Even though it is a secondary effect, the volume force reduction $\mathbf{f}$ may be benefited by an ad-hoc treatment at the tip as done in [4], nevertheless it was not covered in this work.

The force assigned to each cell center contributes to the source term in the right hand side of the momentum balance equation Eq. (7):

$$\frac{\partial \mathbf{u}}{\partial t} + \mathbf{u} \cdot \nabla \mathbf{u} = -\nabla p + \nu \nabla^2 \mathbf{u} + \mathbf{f} \tag{7}$$

In Fig. 1, the flow chart of the process pursued by the coupled CFD-ALM code is depicted. The imposed platform motion is implemented in the CFD-ALM code to simulate FOWT unsteady aerodynamics with prescribed motion according to the load case in Table 2. The position of the actuator points is updated at every time step, corresponding to the instantaneous blade position, and the velocity of the AL points is corrected accordingly using the kinematic laws of the rigid body.

3.2. Velocity sampling method

The novel approach for the velocity sampling in the here-proposed ALM solver aims at delivering a physical-based algorithm that can capture the behavior of the flow close to the force application point, removing analytically the local induction of the bound vortex of the lifting profile. Sampling the velocity directly at the AL point (where the body force is applied) is the method proposed by [3] but steep velocity gradients in the bound vortex region might generate issues of numerical interpolation and lead to solution instability or inaccuracy. Therefore, it was proposed to sample the velocity far apart from the AL point, to enclose completely the bound vorticity of the blade. The algorithm calculates the AoA to each AL point considering only the components laying in the plane orthogonal to the blade axis. Eventually the AoA
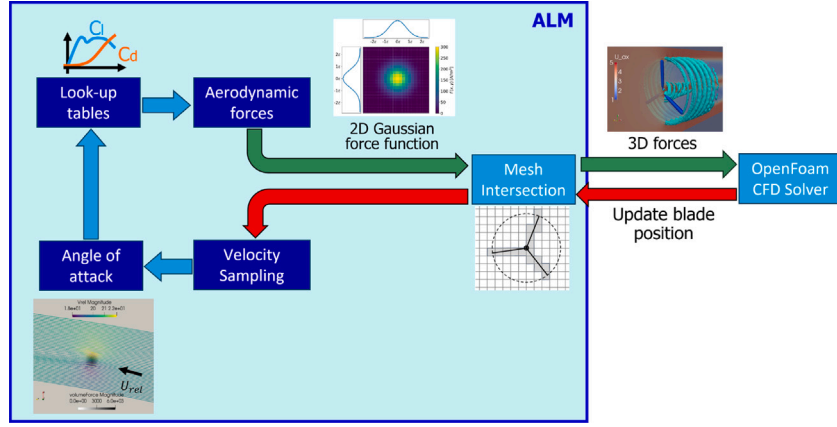
Fig. 1. CFD-ALM algorithm flow chart.

and the velocity magnitude are determined according to Eqs. (3) and (8), using averaged velocity components in axial $\overline{U}_{ax}$ and tangential $\overline{U}_{tg}$ directions.

$$\alpha = \arctan\left(\frac{\overline{U}_{ax}}{\Omega r + \overline{U}_{tg}}\right) - \theta_{pitch} \tag{8}$$

where θ_{pitch} is the local pitch angle and Ωr is the local peripheral speed at the AL point.

Velocity sampling locations are chosen as a function of the rotor average cell size Δ and of the regularization kernel size ϵ. The velocity is sampled on the plane normal to AL also in FOWT cases, therefore the probe locations move according to the turbine motion law. In the following, three alternative sampling methods are discussed, the first two ones (*Line* and *Line Average*) already proposed in literature and used for comparison, and the last one (*Vortex-based*) introduced in this paper.

3.2.1. Line method

The purpose of the Line Method (LM) is to set a straightforward sampling criterion to circumvent the challenges related to the sampling directly at the AL point. LM samples the velocity components along four lines:

- U_{ax} is sampled on a couple of upstream and downstream lines with respect to the AL point, perpendicular to the relative velocity;
- U_{tg} is sampled on a couple of upstream and downstream lines with respect to the AL point, parallel to the relative velocity.

As the direction of the relative velocity is not known a priori, the sampling technique is iterative; this is achieved thanks to the outer loop iteration of the pimple algorithm employed in this code. The left frames of Fig. 2 depict the sampling lines for three sections of the vertical blade in case of surge and pitch motion, for four time steps (the first and the last time instants overlap, except the sampling lines). The lines are $d = 10\Delta$ distant from the AL point and $l = 8\Delta$ long. The distance d is selected to place the lines outside the high velocity gradient region and the length l to average over several points of the fluid domain to smear out local effects.

3.2.2. Line average method

The Line Average method (LA) aims at quantifying the bound vortex effects on the flow field, so to eliminate it from the velocity sampling. The method, devised by [11], requires closed contours, centered at the force application point. The circular contour satisfies the above recommendations and it has been found to be an appropriate solution for the LA method of [11]. The induced velocity generated by the bound vortex is canceled out giving the freestream velocity perceived by the

AL point. Therefore, the free-induction velocity $\mathbf{U}_\infty$ can be determined with Eq. (9), the average over the N_{circ} sampled points for each jth velocity.

$$\mathbf{U}_\infty = \frac{\sum_{j=1}^{N_{circ}} \mathbf{U_j}}{N_{circ}} \qquad j = 1, \dots, N_{circ} \tag{9}$$

The circle has a radius of 10Δ and the number of equispaced sampling points $N_{circ} = 36$ is constant along the blade span. The closed contour radius r has to enclose the whole vorticity of the bound vortex. As matter of fact, the size of the vortex core depends on the kernel size ϵ, hence $r > \epsilon$ must be satisfied (as the kernel has a Gaussian functional form, more than 99% of the force is spread in a circle of radius 3ϵ). In this investigation, it was found that a radius of $r = 5\epsilon$ (with $\epsilon = 2\Delta$) surrounds completely the bound vortex; a detailed analysis of the impact of parameters Δ, ϵ, and r on the numerical solution is proposed in Section 3.3.4. The circles for three generic sections are represented in the central frames of Fig. 2 for surge and pitch motion.

3.2.3. Vortex-based method

The Vortex-Based method (VB) here introduced has been inspired by the work of Shen et al. [8]. The bound circulation Γ of the lifting airfoil is calculated with Eq. (10), using the same sampling points of LA method, namely along a circumference with $r = 5\epsilon = 10\Delta$.

$$\begin{aligned}\Gamma &= \oint_C \mathbf{U} \cdot d\mathbf{s} \\ &= \sum_{j=1}^{N_{circ}} \mathbf{U_{x,j}}\, dx + \sum_{j=1}^{N_{circ}} \mathbf{U_{y,j}}\, dy \quad j = 1, \dots, N_{circ}\end{aligned} \tag{10}$$

The sampling is made on monitor points (MP), which lay on sampling lines normal to the axial direction, upstream and downstream of the rotor plane, shown as red segments in the right columns of Fig. 2. The velocity components induced by the bound vortex, centered in the AL point (x_Γ, y_Γ), on each ith monitor point, placed in coordinates (x_i, y_i), can be analytically calculated with Biot–Savart law according to Eqs. (11) and (12).

$$u_i = \frac{\Gamma}{2\pi} \frac{y_i - y_\Gamma}{(x_i - x_\Gamma)^2 + (y_i - y_\Gamma)^2} \tag{11}$$

$$v_i = \frac{\Gamma}{2\pi} \frac{x_i - x_\Gamma}{(x_i - x_\Gamma)^2 + (y_i - y_\Gamma)^2} \tag{12}$$

$$i = 1, \dots, N_{MP}$$

When the axial and tangential induction velocities (u_i, v_i) are computed, they are subtracted to the local velocity sampled in the MPs and the arithmetic average along the monitor lines is performed, according to Eqs. (13) and (14).

$$\overline{U}_{ax} = \frac{\sum_{i=1}^{N_{MP}} (U_{ax,i} - u_i)}{N_{MP}} \tag{13}$$
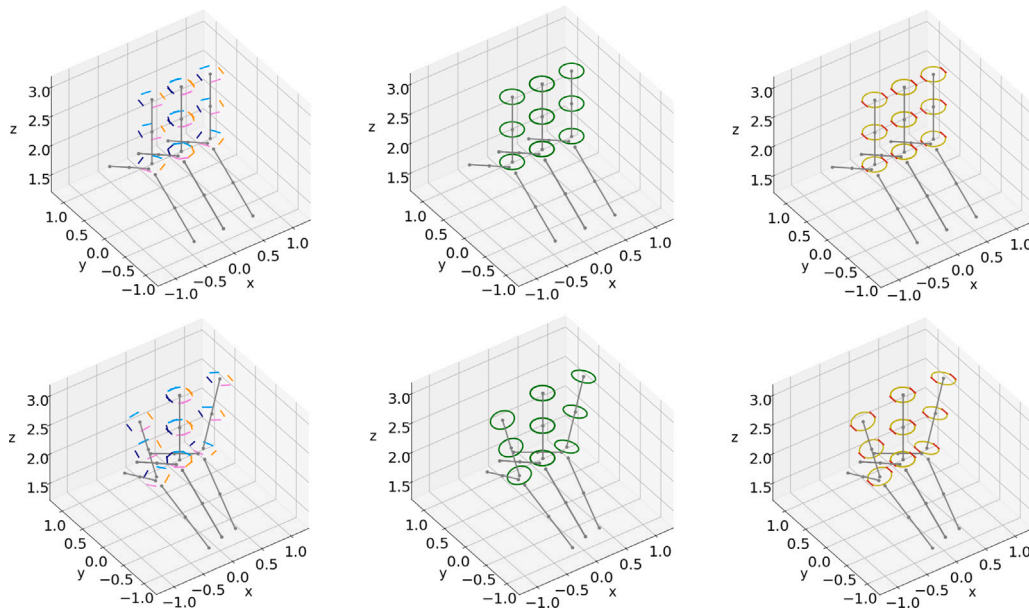
Fig. 2. Sampling techniques applied to different platform motions: Surge (first row), Pitch (second row). Sampling methods: LM (first column), LA (second column), Vortex-Based (third column). Surge and pitch displacements are magnified for explanatory purposes.

Table 3
Parameters for the ALM velocity sampling method.

Method	d [Δ]	l [Δ]	r [Δ]
LM	10	8	–
LA	–	–	10
VB	10	8	10

$$\overline{U}_{tg} = \frac{\sum_{i=1}^{N_{MP}}(U_{tg,i} - v_i)}{N_{MP}} \qquad (14)$$

Finally, the mean between the upstream and downstream averages provides the velocity experienced by the AL point. Sampling lines are placed at distance $d = 10\Delta$ from the AL point and are long $l = 8\Delta$, so to be coherent with the parameters of LM and LA.

Table 3 reports the geometrical parameters for the three sampling strategies. Distance d is the dimension from the AL point (taken as normal to the sampling line), l is the length of each sampling line, r is the radius of the circular path used by LA and VB to sample the velocities from the flow field.

3.3. Numerical set-up

After having presented the physical model, the details of the numerical settings are discussed in this section.

3.3.1. Numerical domain and boundary conditions

The numerical domain reproduces the wind tunnel cross section where the experiments were carried out.

Differently from the physical outflow location, placed at $x = 2.3D$ downstream of the rotor, a longer domain ($x = 14.5D$) was set to avoid spurious reflection at the outflow and to provide sufficient space to develop the wake.

The boundary layer developing at the upper and lower walls of the wind tunnel was not modeled, thus reducing the mesh size. To account for the blockage caused by the boundary layer, while ensuring the experimental mass flow rate, the height of the domain was decreased by the boundary layer displacement thickness, and the walls were modeled with a slip condition, as done in [20].

The lateral walls were simulated with slip wall conditions, like the ceiling and floor of the tunnel, but without any width reduction since

the blockage effect of the rotor is negligible in the rotor-transversal direction.

The velocity profile at the inlet was considered flat, with freestream value equal to $U_0 = 4$ m/s. The same levels of the inlet turbulence measured in the wind tunnel were prescribed to the inflow with a turbulence intensity of 2% and a turbulent length scale of $l_T = 0.1$ m [21]. The atmospheric pressure was imposed at the outlet boundary.

3.3.2. Computational mesh

The mesh was constructed as a background structured grid composed by hexahedrons and features two cylindrical refined mesh regions at the wake and rotor locations; the former starts from $x = 2D$ upstream the rotor and propagates up to the domain outlet with a radius of $1.36R$ (orange region in Fig. 3), the latter encloses the rotor between $x = -0.13D$ and $x = 0.13D$. The average cell size of the coarser mesh (Case A, in Table 5) in the rotor region is $\Delta = 0.017$ m (yellow region in Fig. 3). The grid independence study was carried out by halving the cell dimension in the refinement cylinder of the rotor along three directions, inserting an additional cylinder extending from $x = -0.08D$ to $x = 0.08D$ with a radius of $1.18R$.

3.3.3. Solver

Since the wind turbine model was simulated in the confined environment, the CFD simulation needed a time-resolved approach in order to reproduce the unsteadiness caused by the interaction between the moving blades and the wind tunnel walls, even in case of the fixed-bottom operation. To this end, the time-resolved PIMPLE algorithm was used setting `nOuterCorrectors=2` (outer loops) and `nCorrectors=2` (inner loops) to solve the pressure–velocity coupling. The two outer loops were necessary to provide the iterations needed by the implicit velocity sampling technique, the second outer loop allowing to update the flow field with the recalculated volume force.

A criterion was used to set the minimum time step to resolve the underlying physics of the turbine: the AL must not cross more than one cell while advancing by one time step. The constraint is expressed in Eq. (15), where the number of the time steps over a rotation is $N_{\Delta t}$ and R is the turbine tip radius.

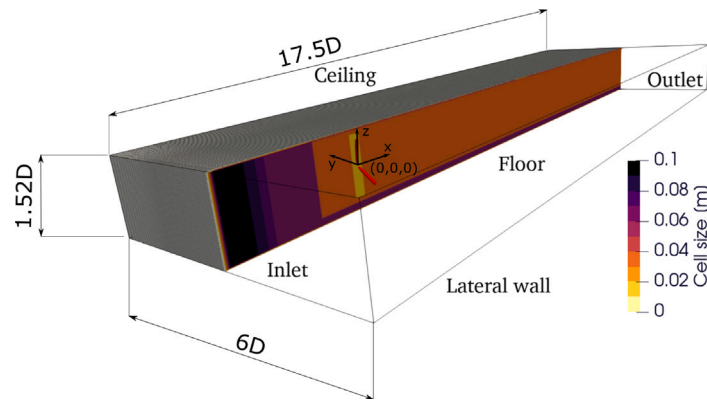$$N_{\Delta t} = \frac{2\pi R}{\Delta} \qquad (15)$$

Fig. 3. Longitudinal section of the CFD domain with boundary conditions: the average cell dimension in plane xz and the iso-contour of the volume forces (red) are shown.

Table 4
Regularization kernel size dependence study.

Case	Δ [m]	ϵ/Δ	r/Δ	ΔF_x [%]	ΔM_x [%]
A	$17 \cdot 10^{-3}$	2	10	–	–
B	$17 \cdot 10^{-3}$	3	10	0.02	0.09
C	$17 \cdot 10^{-3}$	3	15	0.31	0.18

Table 5
Grid independence study.

Case	Δ [m]	ϵ/Δ	r/Δ	ΔF_x [%]	ΔM_x [%]
A	$17 \cdot 10^{-3}$	2	10	–	–
D	$8.7 \cdot 10^{-3}$	4	20	<0.01	<0.01

The selected time step was $\Delta t = 5 \cdot 10^{-4}$ s to ensure $N_{\Delta t} = 500$ as suggested in [22]. The simulated time is 5 s, equal to 20 revolutions of the fixed-bottom turbine, sufficient to reach a periodic solution of thrust and torque. Whereas, FOWT load cases are run for 10 surge and pitch periods to reach a periodic solution with the same time step.

Forces were distributed in the flow field with a 2D Gaussian spreading function on the normal plane to the actuator line, the regularization kernel size ϵ was set as 2Δ as recommended in [22]. According to [23], a convergence with the variation of ϵ cannot be reached.

The effects of turbulence were modeled by resorting to the U-RANS approach, using the $k - \omega$ SST turbulence model. This choice is justified by the specific aim of this study, which is primarily focused on modeling the rotor aerodynamics, with a minor interest in the development and mixing of the far wake. In future studies, the present ALM solver will be used in combination with Large-Eddy Simulation to properly exploit the ALM capability in resolving the wake.

3.3.4. Grid independence
The following analysis was carried out using LA method, to assess the code with a well-established sampling method in literature, and for the fixed-bottom operation.

The purpose of the analysis is twofold:

- to determine the impact of both the parameter ϵ and the size of the sampling radius r (used to calculate velocities in LA and Γ in VB);
- to perform a grid dependence study on the cell size Δ with constant ϵ.

The dependence of the solution from the actuator line parameters was investigated using a baseline mesh whose resolution copes with the best practices of ALM simulations proposed in [24], which indicates that a value of the rotor mesh size $\Delta = R/32$ is sufficient for the grid-independence of the ALM solution. An additional comprehensive grid dependence study was performed by Martinez-Tossas [25], who investigated a wide range of grid resolutions, from $\Delta = R/15$ to $\Delta = R/60$. In

the present study the first mesh was constructed so to already exceed the grid-independent resolution suggested in the literature, namely $\Delta = R/70$, and it was used to investigate the impact of the ratios ϵ/Δ and r/Δ. The grid independence of the solutions obtained with the first mesh was finally carried out, by considering a mesh size refined until $\Delta = R/136$ in the rotor region, obtaining fully consistent results. Cases A, B and C in Table 4 share the same computational grid with average cell dimension in the rotor region $\Delta = 17 \cdot 10^{-3}$ m. This corresponds to an R/Δ ratio of 70 and a total cell count of 11.4 million. In Case A, the ratio $r/\epsilon = 5$ ensures that the closed circular path completely contains the bound vortex, with $\epsilon = 2\Delta$. Case B was built enlarging the regularization kernel $\epsilon = 3\Delta$ but keeping the same sampling radius (ratio $r/\epsilon = 10/3$). Table 4 shows that the increased size of the regularization kernel does not alter the load calculation. This demonstrates that independence to ϵ is achieved for $\epsilon = 2\Delta$, also considering that $\epsilon < 2\Delta$ is not relevant as the Gaussian distribution would result not sufficiently discretized to accurately resolve the bound vortex. Case C features the same setup of Case B, except for a larger value of r, but maintaining the $r/\epsilon = 5$ as Case A. Very minor differences (0.2–0.3%) on thrust F_x and torque M_x are detected with respect to Case A and they are ascribed to the slightly larger contour which may intersect the wake or low momentum regions past the AL point. Hence, the authors suggest to select an optimal value of radius in the range $3 < r/\epsilon < 5$, sufficiently large to contain the whole bound vortex and, simultaneously, the smallest possible to limit the impact of the wake and trailing vortices.

A further comparison to Case D is presented using a finer grid, $\Delta = 8.7 \cdot 10^{-3}$ m, which corresponds to $\Delta = R/136$. This finer mesh is achieved by halving the mesh size within the rotor region of Case A, resulting in a total cell count of 14.6 million. The purpose of the comparison is to assess the grid independence to the refinement. Case D has the same dimensional parameters of case A ($r/\epsilon = 5$), with doubled non-dimensional parameters evaluated with respect to the cell size (ϵ/Δ and r/Δ). Table 5 shows that no differences are observed between Cases A and D. It is highlighted that the grid independence must be carried out with the same absolute dimensional kernel size. In a future work dedicated to the wake resolution, this insight will be useful when refining the numerical domain to resolve the large eddies of turbulence.

Since the coarser grid was found to be independent on r, ϵ and Δ as selected for Case A, these values were used to analyze FOWT load cases. Independence analyses were conducted with LA method only, nevertheless the same conclusions hold true for the VB method as it is based on the calculation of Γ, based on the same closed path used for LA (Eq. (10)).

3.3.5. Time-step dependence analysis
The study on the time-step independence is conducted on Case A, with LA technique, increasing the time step Δt with respect to Case A, still maintaining the Courant number below 1.

Table 6
Time-step dependence study on the fixed-bottom wind turbine model.

Δt [s]	ΔF_x [%]	ΔM_x [%]	max Co	$N_{\Delta t}$
$5 \cdot 10^{-4}$	–	–	0.25	500
$10 \cdot 10^{-4}$	+0.008	+0.022	0.5	250
$15 \cdot 10^{-4}$	+0.053	+0.138	0.75	166

Results in Table 6 show that the rotor load variations are negligible when increasing the time step by a factor three. It is observed that the requirement of the minimum time step is conservative, however the FOWT simulations presented in this paper are run with the smallest time step to match the Courant number requirement in case of mesh refinement. It is also recalled that the use of PIMPLE may relax the constraints on Courant number, however the tighter condition remains the physical one, as per Eq. (15).

4. Results

4.1. Fixed-bottom wind turbine simulation

The fixed-bottom load case LC1.1 was analyzed using the three sampling methods discussed in Section 3.2. The experimental assessment with the UNAFLOW data aimed at validating the velocity sampling methods, which had been subsequently applied to FOWT simulations, presented in Section 4.2.
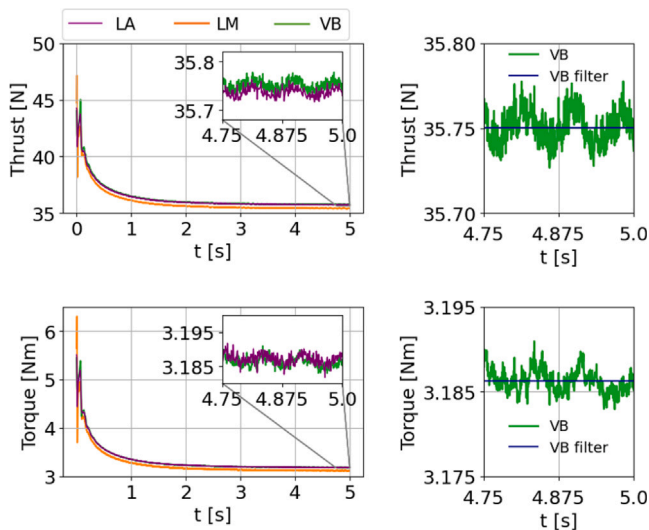

Fig. 4. LC1.1: thrust and torque convergence over simulated time.

The left frames of Fig. 4 shows the convergence history of the rotor thrust and torque values along the simulated time for LA, LM and VB models. The zoomed frame shows the LA and VB signals in the last revolution period to better highlight their small difference. The right frame of Fig. 4 shows the rotor load oscillations given by VB model in the last revolution period $T = 0.25$ s compared to the corresponding filtered signal. The cut-off frequency was set equal to the rotational frequency $f = 4$ Hz to cut the turbine mass imbalance disturbance exciting the revolution frequency in the measurements [14]. The filter was also applied to the ALM data for a direct comparison. The trends of the VB loads show a fluctuation at the blade passing frequency (three times the one of the revolution) caused by the interaction with the wind tunnel walls. The final mean values are obtained by averaging over the last 5 revolution periods and they are listed and compared with the experiment in Table 7 reporting the percentage error referred to the experimental values.

VB and LA methods return similar results both in terms of thrust and torque, with differences from the experiment of the order of 0.5%

Table 7
LC1.1: rotor thrust and torque comparison with experimental data.

LC1.1	Thrust [N]	Torque [Nm]
Exp	35.91	3.320
LM	35.41	3.126
% error Exp	−1.39	−5.85
LA	35.72	3.187
% error Exp	−0.52	−4.00
VB	35.75	3.186
% error Exp	−0.44	−4.03

in terms of thrust and 4% in terms of torque; a slightly higher discrepancy is observed for the LM. Overall, the torque is underestimated with respect to experimental one, with maximum difference of 5.85%, however the absolute difference is within −0.194 Nm.

4.1.1. Blade aerodynamics

The blade-distributed quantities are examined to investigate the behavior of the implemented velocity sampling techniques in detail. Fig. 5 shows the spanwise distributions of AoA, sampled axial velocity and estimated lift coefficient. The trends show that all the sampling methods appear consistent, especially the LA and VB show a remarkable similarity. The main differences are in the root and tip regions.

For radial sections $r/R < 30\%$, due to the cylindrical blade shape and the lack of hub-nacelle system, the fluid deceleration is limited: LA and VB show axial velocities approaching $U_0 = 4$ m/s, while LM is well below with $U_{ax} < 3.5$ m/s. At the inboard blade, larger differences in C_l (peak at $r/R = 0.25$) are the consequence of consistent velocity trends: VB estimates the highest axial velocity, while LM the lowest one. In this portion of the blade the AoA has a steeper gradient and values exceed the static stall limit, so a flow separation on the blade is expected. Any potential contribution of dynamic stall, however, may affect only a narrow radial extent of the blade, in the cylindrical root region, thus supporting the choice of using only static polars in the present simulations.

At blade midspan, the region of maximum thrust extraction of the blade, all velocity sampling models provide the same sampled axial velocity. No significant differences are detected among LM, LA and VB, meaning that the complexity of the fluid behavior, at the hub and tip region, is the major cause of the discrepancies.

The main difference between the methods occurs at the blade tip. In Fig. 5, LA and VB quantities are almost overlapped and are less steep than LM which suddenly increase at the blade tip section. The axial velocity starts increasing at $r/R = 90\%$ and tends to the freestream wind speed. LA and VB achieve higher velocities because the induced velocities are lower. LM sampling is affected by the local effects of the force kernel, which decelerate the flow giving lower U_{ax} values. On the basis of a general knowledge of the flow in the tip region of an horizontal-axis wind turbine, VB and LA appear to better interpret the flow physics of the fixed-bottom turbine; however, in the following FOWTs analyses all the methods will still be proposed, to emphasize the improvement of LA and VB methods.

4.1.2. Verification of vortex-based method

The aim of this section is to verify that the forces computed by the Vortex-Based ALM, by means of the BEM approach, are consistent with the flow field generated by their application. Therefore, the resulting CFD-ALM flow field is used by different engineering techniques to calculate and compare the circulation. Another comparison is performed on the AoAs obtained by the ALM sampling with alternative methods already documented in literature. These methods aim at determining the AoA measuring the velocity close to the blade and assuming that such velocity, responsible of the lift generation, is unknown, hence an iterative procedure is required. However, starting from an ALM solution at convergence, the flow field is already known, therefore no iterative process is required. The following three techniques are considered.
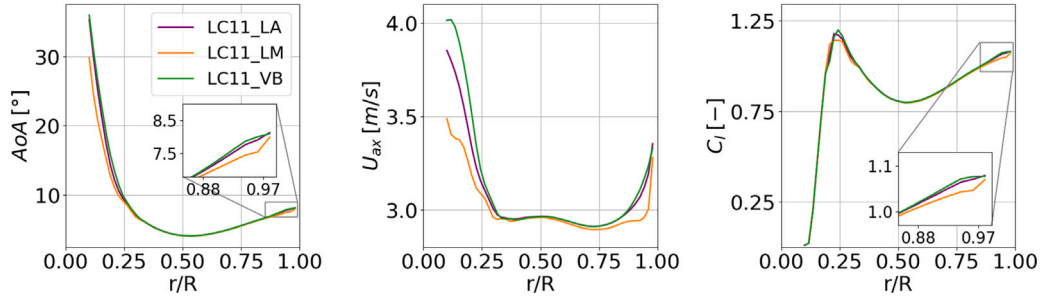
Fig. 5. LC1.1: angles of attack, axial velocity and lift coefficient along the blade span.
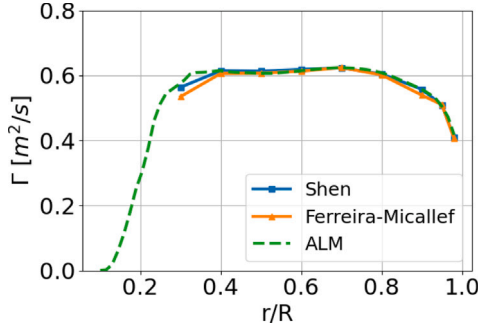

Fig. 6. Comparison of circulation Γ to ALM data, using single point vortex (Shen) and multiple point vortex (Ferreira-Micallef).

Fig. 7. Angle of attack difference computed by engineering methods with respect to ALM results for different CP locations along circumference with radius r = [5,10,15] Δ.

- Single vortex point (referred to as Shen method, [8]): the concentrated bound vortex at the AL point is obtained with Eq. (10) over a circle centered on the AL point. The velocities are sampled on control points (CPs) located on circles tested with different radii. The induced velocities are derived by Biot–Savart law (Eqs. (11)–(12)) on the same CPs. The local velocities are found subtracting induced velocities from sampled ones. The angle of attack is computed with the averaged velocity components.

- Multiple vortex point (referred to as Ferreira-Micallef method, [26]): assuming 2D incompressible flow, the vorticity is considered distributed in the flow field around the AL point, each cell features a discretized parcel of circulation $\Gamma_\omega = \omega_z \Delta x\, \Delta y$. The Biot–Savart matrix with the contribution of each cell-vortex is computed at the CPs located on a circle centered in the AL point. Thus, the velocity value is averaged to find the angle of attack.

- Line Average technique [11]: the velocities are sampled on CPs positioned on a circle centered in the AL point. The contribution of the induced velocity is eliminated by applying an average through the values sampled along the circular symmetrical path, resulting in the required local velocity. This method simply relies on a velocity sampling along an appropriate path and not on the computation of the circulation.

The velocity and vorticity fields of CFD-ALM simulations are extracted at several blade stations along the blade in vertical position at convergence. A sensitivity analysis on the location of CPs is also conducted with three different radii equal to 5Δ, 10Δ, 15Δ to ensure that the verification method is robust for each engineering method. The closed contour with radius 10Δ is employed to calculate the circulation Γ of the concentrated bound vortex (Shen) which guarantees the complete surrounding of the force kernel.

The circulation is derived from the engineering techniques based on the circulation (Shen and Ferreira-Micallef) and compared to ALM value $\Gamma = 0.5\, c\, W\, C_l$. The result, in Fig. 6, demonstrates that the use of a circle of radius $r = 10\Delta$ (Shen) gives a consistent estimate of the circulation.
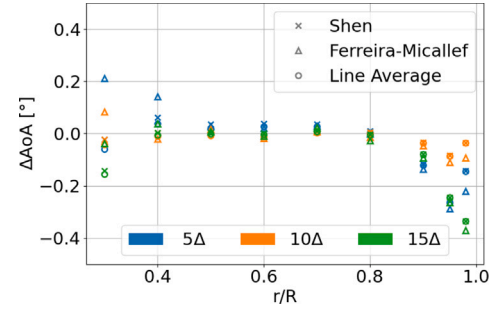
Ferreira-Micallef's modified method shows very similar results, with slightly lower values especially towards the hub. Since the method considers distributed vorticity than a single point vortex, the circulation magnitude may differ especially at the hub, where 3D complex fluid patterns arise, where a thorough calculation of the circulation becomes challenging as strong trailing vortices are shed.

Fig. 7 reports the AoA discrepancies between the three engineering techniques and the VB method computed in Eq. (16):

$$\Delta AoA = \frac{AoA_{VB} - AoA_{eng}}{AoA_{VB}} \qquad (16)$$

The difference is negligible between $r/R > 0.4$ and $r/R < 0.9$. The hub and tip regions exhibit higher differences, which however remain within $\Delta AoA = [0.2, -0.3]°$. In these regions the outputs of the methods are more dispersed, and this can be due to the inherent flow complexity: the location of CPs may indeed influence the velocity sampling because they fall in a region of strong velocity gradients (wake near to the hub) or interact with the trailing vorticity at the tip. Nevertheless, overall results are in very good accordance, since the minor differences in AoAs do not induce any significant change in the aerodynamic performances (the differences are, indeed, even lower than the available discretization of the look-up tables, $0.5°$).

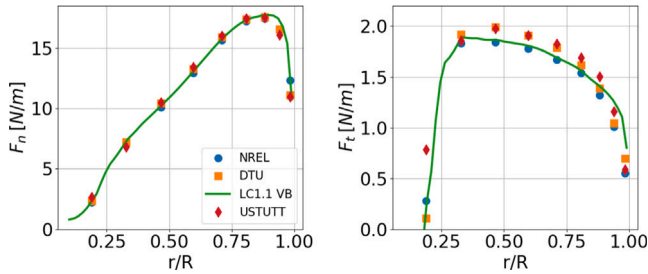### 4.1.3. Numerical assessment against OC6 Phase III models

To broaden the assessment of the ALM in fixed-bottom layout to alternative multi-fidelity prediction tools, the comparison to the models employed in OC6 Phase III is proposed in this section. Data are publicly available at [27]. The participants selected for this numerical comparison cover the whole range of the fidelity levels documented in literature:

- NREL (National Renewable Energy Laboratory) OpenFast, based on the Blade Element Momentum Theory (low fidelity);
- DTU (Technical University of Denmark) HAWC+MIRAS, hybrid Vortex Filament-CFD model (mid fidelity);
- USTUTT (University of Stuttgart) in-house code: Blade-resolved CFD (highest fidelity).

Table 8
LC1.1: rotor thrust and torque comparison with multi-fidelity models of OC6 Phase III.

LC1.1	Thrust [N]	Torque [Nm]
Exp	35.91	3.32
VB	35.75	3.18
% error	−0.44	−4.03
NREL	34.93	3.01
% error	−2.73	−9.34
DTU	35.47	3.19
% error	−1.23	−3.79
USTUTT	35.49	3.34
% error	−1.16	+0.52

Fig. 9. LC1.1: angle of attack along spanwise direction. Comparison with OC6 Phase III results: NREL (BEM) and DTU (CFD-FVW).

Fig. 8. LC1.1: spanwise distribution of the normal force to the rotor plane (F_n) and tangential force in the rotor plane (F_t) of ALM-VB with OC6 Phase III results.

Further details on the models can be found in [14]. In Table 8, only VB results are shown compared to OC6 data, as it represents the newly developed velocity sampling method tailored for FOWT applications.

The ALM-VB model is classified as an intermediate-fidelity code as DTU, and it is found in a closer agreement to it. A source of slight discrepancies in thrust can be due to the modeling of the wind tunnel walls with respect to open field set-up of DTU (despite the simulations with this latter code were performed assigning a higher velocity to compensate the wind tunnel blockage, [14]). NREL finds the lowest values among all the models, while USTUTT, which modeled only a 120 ° sector in open field with hub and nacelle, provides the closest torque estimate to the experiment, while the thrust is in line with the other OC6 participants. It is observed that, with respect to the experiment, the VB model predictions are in-between BEM and blade-resolved CFD, thus respecting the hierarchy of fidelity levels.

An overall agreement between the ALM and intermediate/high-fidelity models was also found in the spanwise distributions of the rotor quantities, with some peculiar differences emerging at the tip, and related to the different treatment of this region in the models. Fig. 8, which reports the spanwise distribution of the force normal to the rotor plane, indicates slightly higher values for the ALM-VB simulation with respect to the ones of the other OC6 models, with an almost perfect overlapping just at the blade extremity, as a consequence of the chord tapering. The tangential force distribution, also reported in Fig. 8, appears in better agreement with BEM, whereas DTU and USTUTT predict higher values throughout the blade span, except at the tip where all the OC6 models get closer and show the reduction of the forces.

To explain the observed trends, the spanwise distribution of AoA values (available for NREL and DTU only) is reported in Fig. 9. The ALM-VB distribution of AoA lays in between the NREL and DTU for most of the blade span, also in the complex hub region. At the blade tip, the AoA distributions for the ALM and DTU models remain monotone (with slightly higher values for the ALM simulation), while the NREL predicted trend drastically reduces. It is to be noted that the BEM formulation of NREL introduces the Prandtl's tip model and also the DTU code accounts for a tip smearing model described in [4]. The
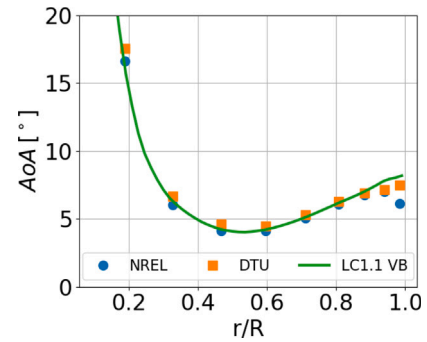
result of the ALM model, in closer agreement with the DTU simulation, confirms that the implementation of a 'full' tip loss model is not needed in the present hybrid BEM-CFD formulation. However, a partial modeling of the tip aerodynamics so to reproduce the integral effect of the pressure equalization towards the tip might be beneficial to slightly improve the fidelity of the ALM simulation, and it will be acknowledged in the future.

4.1.4. Flow field description

The results of the combined experimental and numerical comparison has allowed to verify and validate the proposed ALM model, putting it in the proper ranking in terms of fidelity; especially, the quantitative analysis indicates the effectiveness of the novel sampling technique for evaluating the blade aerodynamics in fixed-bottom condition. To complete the analysis, it is interesting to investigate the flow field reproduced by the ALM in fixed-bottom condition (LC1.1), to verify the physical significance of the method.

The flow field is analyzed for all the three methods implemented in the ALM code (LM, LA, VB), selecting as representative blade section the one at $r/R = 70\%$ (for the blade placed in vertical position). Fig. 10 reports the axial and tangential velocity components normalized by the free-stream velocity of the CFD solution at convergence of LM and LA velocity sampling methods. The black dotted lines mark the velocity sampling locations for the two methods. The incoming flow is directed from left to right and the rotational speed imparts a clockwise rotation (looking from upwind) of ALs with the rotor axis oriented in positive x direction.

The distribution of the velocity field copes with the distribution of the forces, according to a regularization kernel, which imparts a vortex-like induction field with a rotational core surrounded by a two-lobe irrotational pattern. It is observed that, between the two methods, the velocity flow field is qualitatively equivalent for both axial and tangential components, therefore the main difference in the estimate of the integral loads and blade-distributed quantities resides in the evaluation of the magnitude and direction of the velocity vector through the velocity sampling methods. The LM samples in upstream and downstream regions of the AL point along U_{rel} direction on a 8Δ-length line. Therefore, it turns out very sensitive to low momentum flow in the trailed vortex region characterized by lower values, which tend to decrease U_{ax} as documented by Fig. 5. The axial velocity in the LA method is averaged over a circular contour where the induction contributions are intended to be canceled out. The result estimates a higher induction at the tip and lower at the hub as in Fig. 5. Sampling over a symmetrical contour turns out a more reliable model with respect to LM, since it predicts more physical trends at the hub and the tip, where the LM is sensitive to the highly complex flow phenomena.

The interpretation of VB method is worth of consideration because it illustrates the combination of the sampling of the velocity and the elimination of the induced velocity, with the aim to give induction-free
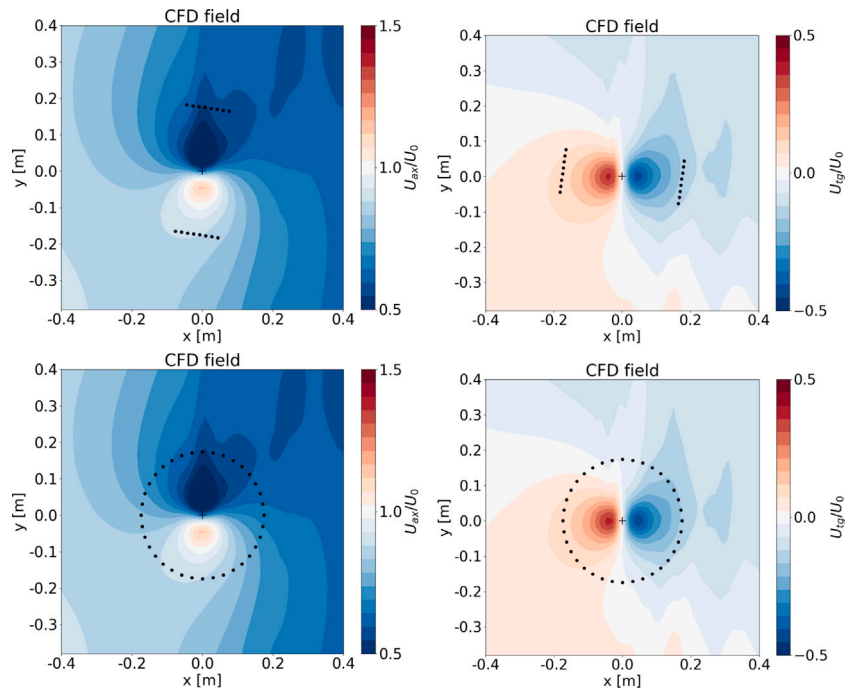
Fig. 10. LC1.1: axial (left frames) and tangential (right frames) velocity components at blade section 70% of the blade span for LM (first row) ad LA (second row).

velocity components. Fig. 11 sheds light on the method implemented in the ALM-VB. The CFD flow field obtained by ALM code (left frames of Fig. 11) can be seen as the superimposition of two flow fields: (i) the induction field generated by the bound vortex (central frames of Fig. 11) and (ii) the global velocity field induced by the turbine in the streamtube crossing the rotor (right frames of Fig. 11).

The induced velocity field reported in the figure is reconstructed assuming a point-vortex acting on the AL point, under the assumption of incompressible, rotational, 2D flow. This analytical model introduces an approximation of the velocities close to the AL point which constitutes a singularity for distances from the vortex center tending to zero. Values tending to infinity are avoided by the inherent finite discretization of the numerical domain.

Subtracting the CFD velocity field by the vortex-induced distribution, the field generated by the global induction of the rotor is obtained, thus representing the momentum variation introduced by the wind turbine having mostly eliminated the local effects of the bound vortex. The resulting axial velocity U_{ax} field evidences the velocity decrease across the rotor as predicted by the 1D momentum equation balance.

In fact, the point-vortex approximation affects the bound-vortex-free field close to AL point, which shows the pattern of a doublet with flipped peaks with respect to the induction velocities. This perturbation is caused by the fact that in the ALM code the bound vorticity is not applied as a point-vortex, since the aerodynamic force is not applied in one point, but it is spread by the regularization kernel. However, the assumption of point vortex core does not affect the sampling of the velocity, since the sampling line locations are placed at 5ϵ, far apart from the residual perturbation resulting from the combination of a point-wise vortex with a distributed force.

An improved implementation of the code could involve the calculation of the induced velocity according to a distributed vortex-core model (e.g. "Scully" or "Lamb-Oseen" vortex), so that the free-induction CFD field does not show the doublet pattern at the vortex center. Anyhow this implementation would not change the outcome of the sampling having placed the sampling lines at a sufficiently high distance from the residual perturbation zone.

The same treatise applies for tangential velocities of the bound vortex free field, the doublet is still present at the AL point and

velocity gradients develop perpendicularly to the one found for the axial components with more disturbances related to the trailing vortex passage.

It is demonstrated that the approach based on the vortex model combined with a method which samples upstream and downstream velocities at the rotor exhibits a numerical robustness and physical reliability when the sampling at the MPs occurs outside the regularization kernel, as done in this work.

4.2. FOWT simulation results

After having validated and analyzed the proposed ALM code for a conventional fixed-bottom turbine, the load cases with surge and pitch platform motion are illustrated in this Section.

A low-pass filter with cut-off at 3 Hz was used, in the surge experiment, to purge the experimental signal of thrust and torque from the disturbances, therefore the same filter has been applied to the ALM values for coherence. A combined experimental-computational assessment is provided for the surge case (LC2.5) in Section 4.2.1; a computational assessment is discussed for the pitch case (LC3.5) in Section 4.2.2.

4.2.1. Surge platform motion

Thrust and torque integral values reach a periodic solution for the surge case, as clearly visible in the left frames of Fig. 12. The zoomed frame shows the LA and VB signals in the last surge period to better highlight their small difference. The right frame of Fig. 12 shows the rotor load oscillations given by VB model in the last surge period $T = 1$ s compared to the corresponding filtered signal.

In Fig. 13, thrust and torque trends are visualized along a single surge platform period and Table 9 reports the mean and amplitude values with their experimental counterparts. The percentage errors computed in this paper for the mean and peak-to-peak amplitude values are expressed as percentage of the mean experimental values, according to Eq. (17).

$$errorMean = \frac{|mean(ALM) - mean(EXP)|}{mean(EXP)} \cdot 100$$

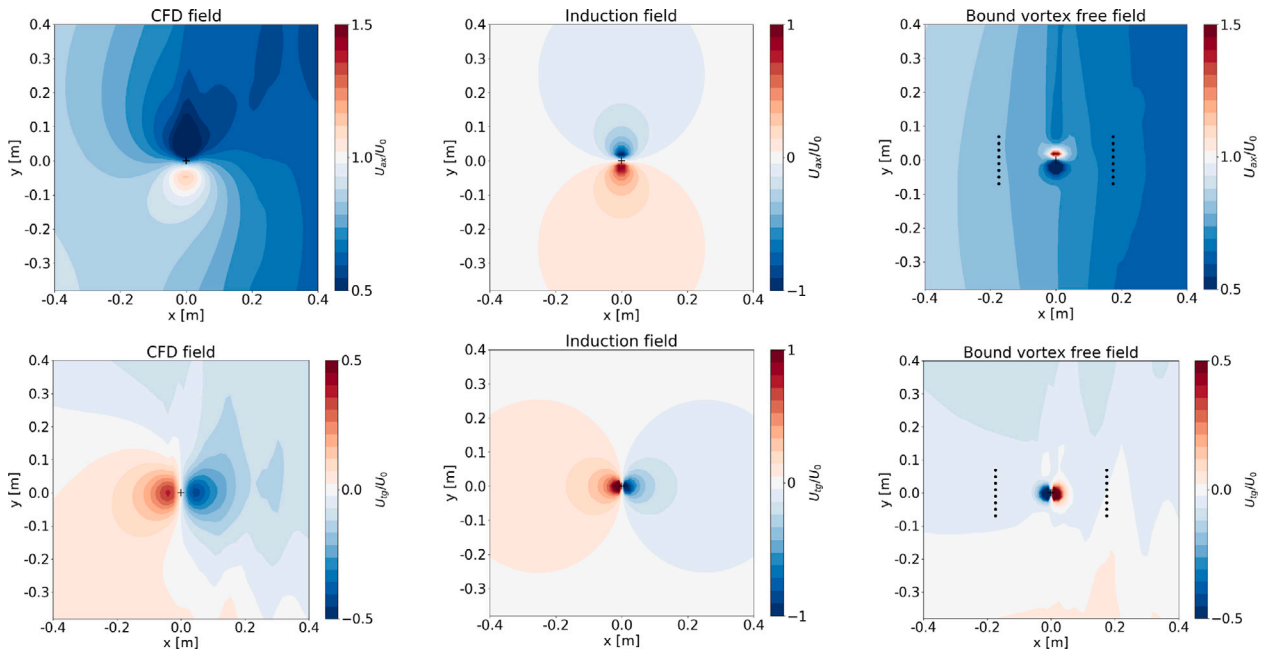$$errorAmplitude = \frac{|ampl(ALM) - ampl(EXP)|}{mean(EXP)} \cdot 100$$

(17)

Fig. 11. LC1.1: ALM-VB axial and tangential velocity fields at blade section 70% of the blade span. CFD flow field and induced flow field by the bound-vortex and free-induced velocity field.
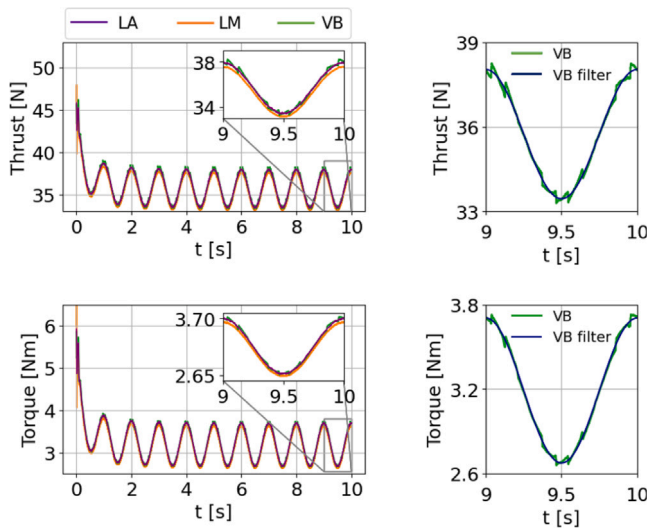

Fig. 12. LC2.5: thrust and torque periodic solution over simulated time.

Fig. 13. LC2.5: hub displacement, thrust and torque comparison with experiments Exp (dashed black) in surge platform motion. Filtered ALM results (solid lines) and mean values (dotted lines) are shown.

The ALM and experimental loads find mean thrust and torque values close to fixed bottom case, suggesting that the combination of frequency and amplitude of the platform examined for this load case does not alter the mean operation of the turbine with respect to fixed-bottom operation.

The three methods produce thrust results in agreement with the experiments for both mean and amplitude values, with percentage errors reported in Table 9. The numerical simulations show larger deviations, and in general an underestimate, of torque values, within −7.8% (mean) and −4.1% (amplitude). Despite appearing large in percentage, these differences in torque are small in absolute values, especially considering the load-cell uncertainty resulting from of the inertia subtraction process described in [20]. Among the ALM methods implemented in this study, the LA and VB give similar results, in better agreement with the experiment with respect to the LM as depicted in Fig. 13.
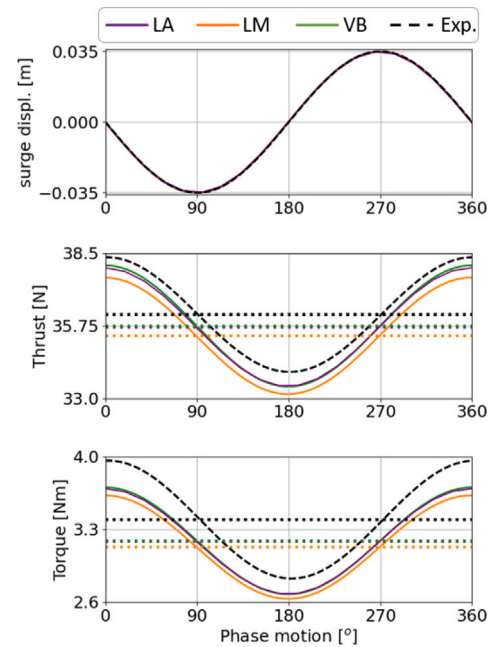
For the following analyses only the novel ALM-VB is considered for the assessment against multi-fidelity codes.

The ALM-VB predictions are compared to those obtained by a selection of OC6 Phase III participants, introduced in Section 4.1.3, in Fig. 14. The quantitative comparison of Table 10 shows that VB method achieves coherent values with OC6 Phase III participants, the percentage errors of ALM-VB are in the range of low- and high-fidelity models.

The overall outcome of the experimental assessment is in sound agreement between numerical and experimental results, especially for
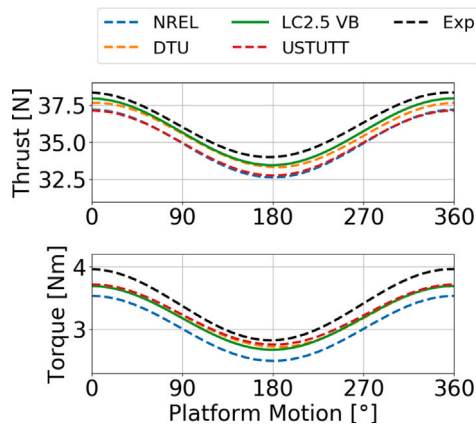
Fig. 14. LC2.5: thrust and torque over a surge period. Comparison with OC6 Phase III results.

Table 9
LC2.5: rotor thrust and torque comparison with experimental data.

Load case	Thrust [N]		Torque [Nm]	
	Mean	Ampl.	Mean	Ampl.
Exp	36.17	4.34	3.39	1.14
LM	35.37	4.41	3.13	0.996
% error	−2.22	+0.19	−7.80	−4.10
LA	35.70	4.48	3.18	1.02
% error	−1.31	+0.40	−6.19	−3.50
VB	35.74	4.59	3.19	1.03
% error	−1.19	+0.68	−6.01	−3.15

Table 10
LC2.5: rotor thrust and torque comparison with experimental data and OC6 numerical models [17] and [27].

Load case	Thrust [N]		Torque [Nm]	
	Mean	Ampl.	Mean	Ampl.
Exp	36.17	4.34	3.39	1.14
VB	35.74	4.59	3.19	1.03
% error	−1.19	+0.68	−6.01	−3.15
NREL	34.98	4.55	3.02	1.04
% error	−3.30	+0.59	−10.89	−2.85
DTU	35.55	4.32	3.22	0.99
% error	−1.72	−0.06	−5.08	−4.24
USTUTT	35.01	4.37	3.25	0.96
% error	−3.20	+0.08	−4.38	−5.17

the thrust mean and amplitudes; the higher torque deviations may be affected by a slight over-speed of the rotor due to the non-perfectly rigid controller detected during UNAFLOW campaign [14].

Fig. 15 shows the variability of the angle of attack and the relative velocity perceived by the rotor for four instants [0, 1/4, 1/2, 3/4] *T* of the surge platform period. The relative velocity is computed as the difference between the axial sampled velocity and the platform one, $W_{ax} = U_{ax} - U_{plat}$. The ALM-VB method follows a linear variation over time with maximum and minimum AoA and W_{ax} at $t = 0$ *T* and $t = 1/2$ T, corresponding to windward and leeward phases, respectively. It is interesting to note that the fixed-bottom condition coincides with the surge one at instants $t = 1/4$ *T* and $t = 3/4$ T, thus highlighting the linear character of the perturbation induced by the surge motion.

After having discussed the integral load data predicted by the ALM code, it is interesting to investigate the flow field reproduced by the model. Fig. 16 shows the flow field around the AL point for two blade sections at $r/R = 70\%$ and $r/R = 95\%$; for each blade section, four instants are reported, two for each frame; to better appreciate the flow unsteadiness, the two instants are shifted by half a period.
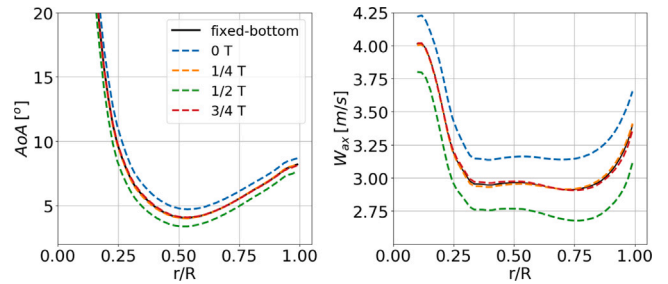

Fig. 15. LC2.5: span-wise angle of attack and relative axial velocity for 4 instants during the surge period *T*.

Table 11
LC2.5: AoA mean value and amplitude for blade sections at r/R = 33, 47, 71, 94%. Comparison with other participants to OC6 project [17] and [27].

		Mean AoA [°]	Ampl. AoA [°]
$r/R = 33\%$	*VB*	6.32	1.88
	NREL	6.06	1.75
	DTU	6.06	1.66
$r/R = 47\%$	*VB*	4.24	1.44
	NREL	4.15	1.43
	DTU	4.45	1.40
$r/R = 71\%$	*VB*	5.13	1.17
	NREL	5.05	1.26
	DTU	5.20	1.11
$r/R = 94\%$	*VB*	7.82	1.09
	NREL	7.03	1.03
	DTU	7.02	0.89

We first consider the left frames of Fig. 16. These frames report the flow configuration at the beginning (solid line) and at the half (dashed line) of the period, when the turbine is in the same position $x = 0$ m but in the windward and leeward phase motion respectively. The contour plots evidence noticeable differences between the two instants. At time $t = 0$ *T* the contour levels show higher absolute values of maximum and minimum flow velocities in the doublet with respect to the ones at t=1/2 T. This is coherent with the forces shown in Fig. 13. At radial section $r/R = 95\%$ the differences are even more visible in the source of the doublet, $U_{ax} > 0.65$ m/s, than in the sink, and in the region downstream of the rotor, where the tip vortex contours are different due the to different convection velocities in the wake resulting from the turbine surge motion.

The right frames, at $t = 1/4$ *T* and $t = 3/4$ *T*, depict the blade sections when the turbine is located at its maximum forward and backward position. The two time instants feature the same apparent wind; therefore, the loads match in presence of a quasi-steady behavior. As matter of fact, the contour levels nearly overlap, unless for the shifted turbine position of $\Delta x = 2 A_s = 0.07$ m due to different AL point positions. Moving downstream ($x > 0$), differences arise due to the different wake structure, visible at $r/R = 0.95\%$ observing the tip vortices.

The assessment to OC6 Phase III results includes an analysis on AoA variation over a surge period for four different sections $r/R = [0.33, 0.47, 0, 71, 0.94]$. Fig. 17 shows the VB method in comparison to NREL and DTU available data. The angle of attack presents a sinusoidal trend over time aligned with the apparent wind. The quantitative AoA means and amplitudes are reported in Table 11. The VB method and the OC6 predictions show coherent results for the most of the blade span, the major differences being detected at the tip where the VB method does not include a dedicated tip loss model, thus both mean and amplitude values turn out higher than OC6 Phase III counterparts.

4.2.2. Pitch platform motion
This section proposed a numerical assessment of in-house ALM code against selected OC6 Phase III results for pitch platform motion case
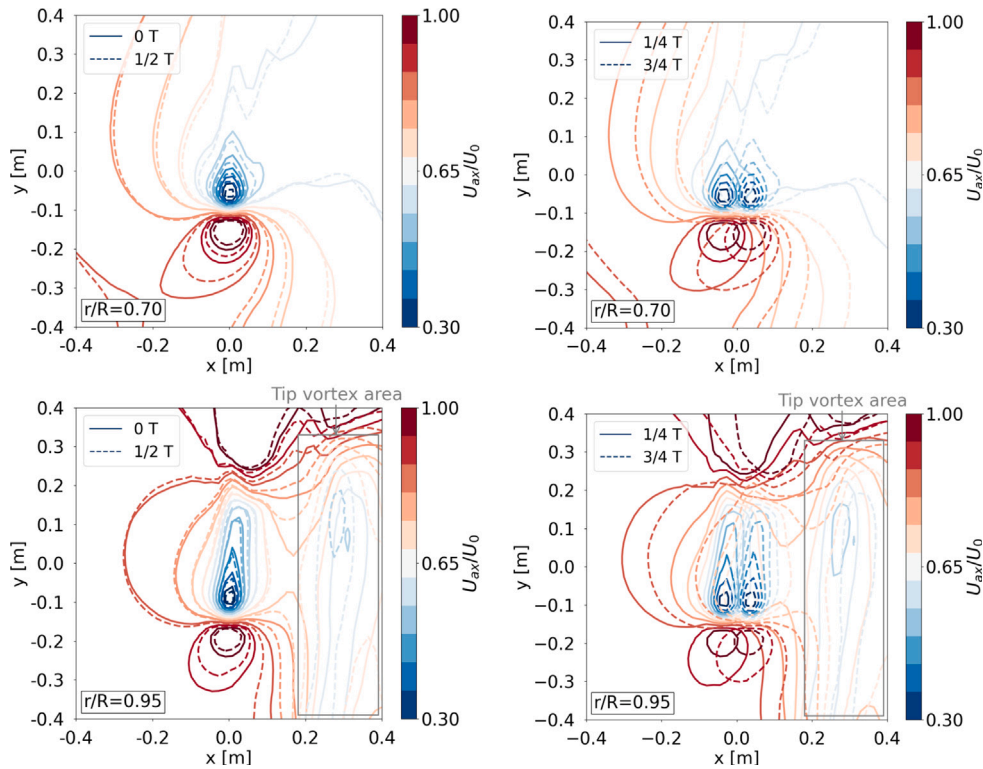
Fig. 16. LC2.5: normalized axial velocity flow field at four time steps during surge at blade sections $r/R = 70\%$ and $r/R = 95\%$. Incoming wind from left.
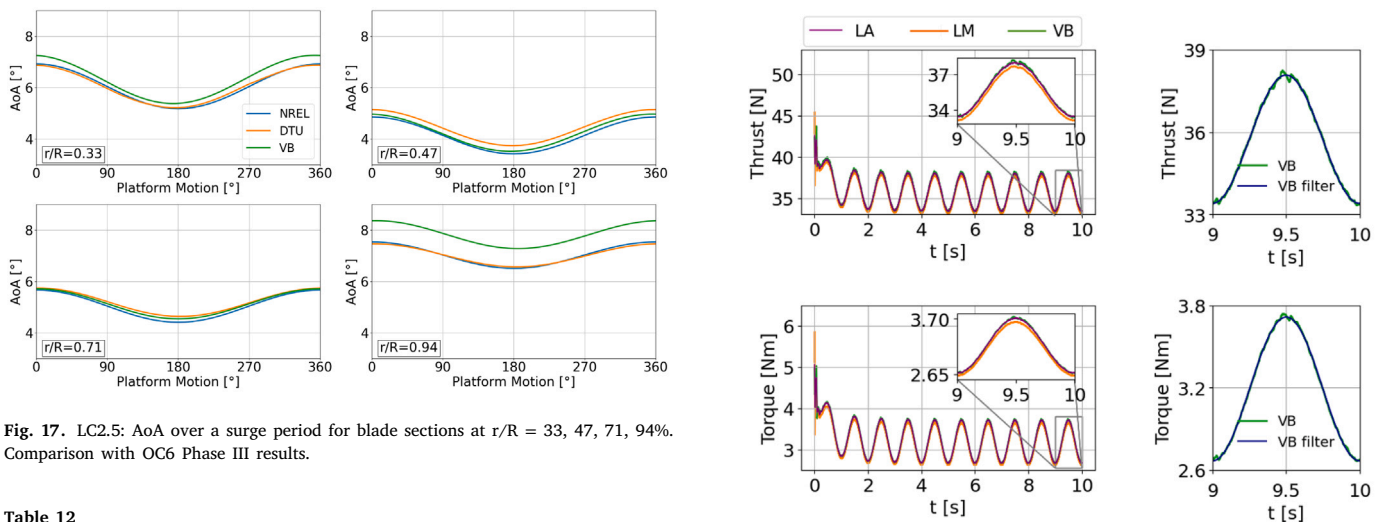

Fig. 17. LC2.5: AoA over a surge period for blade sections at $r/R = 33, 47, 71, 94\%$. Comparison with OC6 Phase III results.

Table 12
LC3.5: rotor thrust and torque comparison with OC6 numerical models [17] and [27].

Load case	Thrust [N]		Torque [Nm]	
	Mean	Ampl.	Mean	Ampl.
LM	35.37	4.54	3.13	1.01
LA	35.69	4.56	3.19	1.04
VB	35.74	4.67	3.19	1.05
NREL	34.85	4.64	3.00	1.06
DTU	35.07	4.44	3.12	1.01

Fig. 18. LC3.5: thrust and torque convergence over simulated time.

LC3.5. The numerical simulation was run for 10 s to achieve a periodic solution as shown in Fig. 18.

Fig. 19 depicts thrust and torque trend over a complete pitch period comparing the VB method with the available data from OC6 models. In Table 12, ALM-VB is found in good agreement with NREL and DTU for both thrust and torque amplitudes. The percentage difference of thrust and torque amplitudes between the average among OC6 participants and VB method is 2.8% for thrust and 1.2% for torque. Slightly larger differences are instead visible for the mean values of thrust and torque. The dispersion between the thrust and torque mean values is 2.2% and 4.3% respectively.
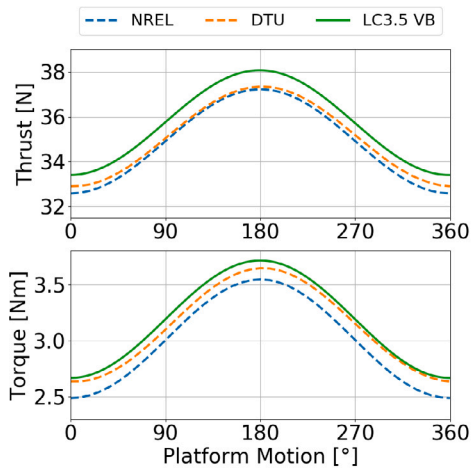
Fig. 19. LC3.5: thrust and torque over one pitch period. Comparison with OC6 Phase III results.
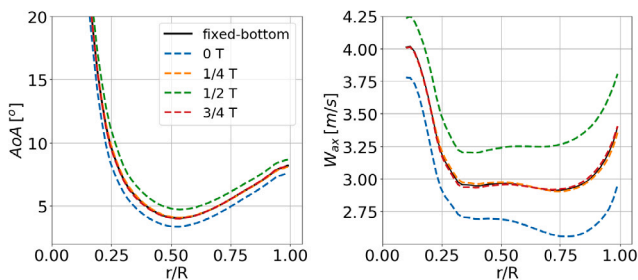

Fig. 20. LC3.5: span-wise angle of attack and relative axial velocity for 4 instants during the pitch period T.

The comparison among the computed trends, in absence of experiments, is particularly challenging and demands a careful analysis. Taking into consideration the fixed-bottom and surge cases, previously analyzed, it can be observed that the VB method, as well as the NREL results, exhibits a remarkable coherence between the LC1.1, LC2.5 and LC3.5 cases, providing almost identical values of mean thrust and torque among the different load cases. This behavior is assumed to be correct given the linearity of the (relatively weak) disturbance generated by the platform motion. For the fixed-bottom and surge cases, the mean values provided by the VB method are closer to the experimental data and always greater than those obtained from the NREL simulations. Therefore, the higher mean thrust and torque values estimated by the VB method also for the pitch case can be assumed coherent and consistent with what has already been observed and validated with the experiments in the previous cases. Instead, the comparison with the DTU data is more difficult because the DTU simulations exhibit a wider variation of mean thrust and torque values among the LC1.1, LC2.5, and LC3.5 cases. This specific behavior, combined with the absence of high-fidelity CFD simulation results, makes it difficult to draw further conclusions.

Overall, the new proposed ALM-VB approach shows good agreement with multi-fidelity code validation in pitch platform motion.

As previously proposed for the surge platform motion, an analysis of the AoA and relative axial velocity radial distributions during the period is proposed also for pitch platform motion. Four time steps uniformly distributed over the last simulated pitch period are considered in Fig. 20 (it is recalled here that the turbine pitching motion is shifted by half a period with respect to the surge motion). The angle of attack excursions of $\Delta\alpha \approx 1.5°$ are symmetric to fixed-bottom value, however the relative axial velocity distribution over the blade span is

different from the one found in surge load case: the pitch platform motion induces an asymmetric loading on the rotor with respect to plane xz; as a result, the blade stations more distant from the pitching center of rotation undergo a higher apparent wind producing bigger excursions of W_{ax} at the tip. This effect is not visible in the amplitude of the attack angle because of the contribution given by the peripheral speed. As in the surge case, also the pitch motion behaves like a linear perturbation generating the fixed-bottom trend for AoA and W_{ax} at the motion extremes (t=1/4 T and t = 3/4 T). The assumption regarding the quasi-steady motion condition is confirmed by the superimposition between the curves of the instants of maximum unsteadiness and the fixed-bottom case.

These observations demonstrate that the implemented ALM code is able to capture the main physical behaviors expected from the tested motion condition.

5. Conclusions

This paper has presented a novel computational tool for the simulation of floating off-shore wind turbines, based on an actuator-line modeling of the rotor and implemented in the frame of a well-established computational fluid-dynamic framework. The key feature of the method is the novel velocity sampling technique, based on the calculation of the bound vorticity obtained from the evaluation of the circulation in the computed flow field around the actuator point. Subtracting the velocity induced by the bound vortex from the CFD flow, a bound-vortex-free velocity field is obtained, which makes the sampling accurate and robust. This so-called Vortex-Based method was verified against alternative and well-established sampling techniques, and it has been proved to be reliable, both qualitatively and quantitatively.

The actuator-line code was then validated against experimental data achieved in the frame of the UNAFLOW test campaign, in which a laboratory model of an HAWT was tested in fixed-bottom and floating operating conditions; moreover, the simulations were compared to calculations performed, for the same turbine, with alternative computational models, in the frame of the OC6 Phase III project. The experimental and numerical assessments showed sound agreement, placing the present code in the proper ranking of fidelity levels, namely in-between momentum-balance integral methods and blade-resolved CFD models. The simulations performed with the floating motions demonstrated the capability of the proposed code to treat properly both surge and tower pitch motion, thus making the code a powerful tool for rotor simulations in dynamic operation.

This work has demonstrated the capability of the proposed ALM code to obtain reliable rotor load predictions for cases featuring Windmill State. Extreme load cases, implying Turbulent Wake State and Vortex-Ring State were not included in this paper due to the lack of experimental data to validate the present ALM. By virtue of the CFD-based modeling of the wake, a high-fidelity prediction of the far wake development and mixing will also be possible in the context of the ALM code by resorting to a Large-Eddy-Simulation formulation for the turbulence modeling. This is the most relevant future development of this work, and it will pave the way for the investigation of wind farms featuring multiple turbines, in both on-shore and off-shore layouts.

CRediT authorship contribution statement

Andrea G. Sanvito: Writing – review & editing, Writing – original draft, Validation, Software, Methodology, Investigation, Formal analysis, Data curation, Conceptualization. **Agnese Firpo:** Writing – review & editing, Writing – original draft, Validation, Software, Methodology, Investigation, Formal analysis, Data curation, Conceptualization. **Paolo Schito:** Writing – review & editing, Supervision, Software, Investigation, Formal analysis, Conceptualization. **Vincenzo Dossena:** Writing – review & editing, Supervision, Resources, Project administration, Investigation, Funding acquisition, Conceptualization. **Alberto**

Zasso: Writing – review & editing, Validation, Project administration, Investigation, Conceptualization. **Giacomo Persico:** Writing – review & editing, Writing – original draft, Supervision, Methodology, Investigation, Formal analysis, Conceptualization.

Declaration of competing interest

The authors declare that they have no known competing financial interests or personal relationships that could have appeared to influence the work reported in this paper.

Acknowledgments

References

[1] A. Otter, J. Murphy, V. Pakrashi, A. Robertson, C. Desmond, A review of modelling techniques for floating offshore wind turbines, Wind Energy 25 (5) (2022) 831–857, http://dx.doi.org/10.1002/we.2701, URL https://onlinelibrary.wiley.com/doi/abs/10.1002/we.2701.

[2] J.N. Sorensen, W.Z. Shen, Numerical modeling of wind turbine wakes, J. Fluids Eng. 124 (2) (2002) 393–399, http://dx.doi.org/10.1115/1.1471361.

[3] R. Mikkelsen, Actuator Disc Methods Applied to Wind Turbines (Ph.D. thesis), in: MEK-FM-PHD, (2003–02) Technical University of Denmark, 2004.

[4] A.R. Meyer Forsting, G.R. Pirrung, N. Ramos-García, A vortex-based tip/smearing correction for the actuator line, Wind Energy Sci. 4 (2) (2019) 369–383, http://dx.doi.org/10.5194/wes-4-369-2019, URL https://wes.copernicus.org/articles/4/369/2019/.

[5] M.J. Churchfield, S. Schreck, L.A. Martinez-Tossas, C. Meneveau, P.R. Spalart, An advanced actuator line method for wind energy applications and beyond, AIAA 1998 (2017) (2017) 20, http://dx.doi.org/10.2514/6.2017-1998, URL https://www.osti.gov/biblio/1358343, 35th Wind Energy Symposium.

[6] L.A. Martínez-Tossas, M.J. Churchfield, C. Meneveau, Optimal smoothing length scale for actuator line models of wind turbine blades based on Gaussian body force distribution, Wind Energy 20 (6) (2017) 1083–1096, http://dx.doi.org/10.1002/we.2081, URL https://onlinelibrary.wiley.com/doi/abs/10.1002/we.2081.

[7] H. Lu, F. Porté-Agel, Large-eddy simulation of a very large wind farm in a stable atmospheric boundary layer, Phys. Fluids 23 (6) (2011) 065101, http://dx.doi.org/10.1063/1.3589857.

[8] W. Shen, M. Hansen, J. Sørensen, Determination of angle of attack (AOA) for rotating blades, in: Wind Energy, Springer Verlag, Germany, 2006, pp. 205–209, URL http://www.forwind.de/euromech/, EUROMECH Colloquium 464b: Wind Energy : International Colloquium on Fluid Mechanics and Mechanics of Wind Energy Conversion ; Conference date: 04-10-2005 Through 07-10-2005.

[9] W.Z. Shen, M.O.L. Hansen, J.N. Sørensen, Determination of the angle of attack on rotor blades, Wind Energy 12 (1) (2009) 91–98, http://dx.doi.org/10.1002/we.277, URL https://onlinelibrary.wiley.com/doi/abs/10.1002/we.277.

[10] A. Arabgolarcheh, S. Jannesarahmadi, E. Benini, Modeling of near wake characteristics in floating offshore wind turbines using an actuator line method, Renew. Energy 185 (2021) 871–887, http://dx.doi.org/10.1016/j.renene.2021.12.099.

[11] E. Jost, L. Klein, H. Leipprand, T. Lutz, E. Krämer, Extracting the angle of attack on rotor blades from CFD simulations, Wind Energy 21 (10) (2018) 807–822, http://dx.doi.org/10.1002/we.2196, URL https://onlinelibrary.wiley.com/doi/abs/10.1002/we.2196.

[12] P.F. Melani, F. Balduzzi, G. Ferrara, A. Bianchini, Tailoring the actuator line theory to the simulation of vertical-axis wind turbines, Energy Convers. Manage. 243 (2021) 114422, http://dx.doi.org/10.1016/j.enconman.2021.114422.

[13] A. Fontanella, I. Bayati, R. Mikkelsen, M. Belloli, A. Zasso, UNAFLOW: A holistic wind tunnel experiment about the aerodynamic response of floating wind turbines under imposed surge motion, Wind Energy Sci. 6 (5) (2021) 1169–1190, http://dx.doi.org/10.5194/wes-6-1169-2021, URL https://wes.copernicus.org/articles/6/1169/2021/.

[14] R. Bergua, A. Robertson, J. Jonkman, E. Branlard, A. Fontanella, M. Belloli, P. Schito, A. Zasso, G. Persico, A. Sanvito, E. Amet, C. Brun, G. Campaña-Alonso, R. Martín-San-Román, R. Cai, J. Cai, Q. Qian, W. Maoshi, A. Beardsell, G. Pirrung, N. Ramos-García, W. Shi, J. Fu, R. Corniglion, A. Lovera, J. Galván, T.A. Nygaard, C.R. dos Santos, P. Gilbert, P.-A. Joulin, F. Blondel, E. Frickel, P. Chen, Z. Hu, R. Boisard, K. Yilmazlar, A. Croce, V. Harnois, L. Zhang, Y. Li, A. Aristondo, I. Mendikoa Alonso, S. Mancini, K. Boorsma, F. Savenije, D. Marten, R. Soto-Valle, C.W. Schulz, S. Netzband, A. Bianchini, F. Papi, S. Cioni, P. Trubat, D. Alarcon, C. Molins, M. Cormier, K. Brüker, T. Lutz, Q. Xiao, Z. Deng, F. Haudin, A. Goveas, OC6 project phase III: validation of the aerodynamic loading on a wind turbine rotor undergoing large motion caused by a floating support structure, Wind Energy Sci. 8 (4) (2023) 465–485, http://dx.doi.org/10.5194/wes-8-465-2023, URL https://wes.copernicus.org/articles/8/465/2023/.

[15] I. Bayati, M. Belloli, L. Bernini, D. Boldrin, K. Boorsma, M. Caboni, M. Cormier, R. Mikkelsen, T. Lutz, A. Zasso, UNAFLOW project: Unsteady aerodynamics of floating wind turbines, J. Phys. Conf. Ser. 1037 (7) (2018) 072037, http://dx.doi.org/10.1088/1742-6596/1037/7/072037.

[16] I. Bayati, M. Belloli, LucaBernini, A. Zasso, Aerodynamic design methodology for wind tunnel tests of wind turbine rotors, J. Wind Eng. Ind. Aerodyn. (167) (2017) 217–227.

[17] A. Robertson, R. Bergua, A. Fontanella, J. Jonkman, OC6 phase III definition document, 2023, http://dx.doi.org/10.2172/1957538, URL https://www.osti.gov/biblio/1957538.

[18] T. Sebastian, M. Lackner, Analysis of the induction and wake evolution of an offshore floating wind turbine, Energies 5 (4) (2012) 968–1000, http://dx.doi.org/10.3390/en5040968, URL https://www.mdpi.com/1996-1073/5/4/968.

[19] R. Kyle, W.-G. Früh, The transitional states of a floating wind turbine during high levels of surge, Renew. Energy 200 (2022) 1469–1489.

[20] S. Mancini, K. Boorsma, M. Caboni, M. Cormier, T. Lutz, P. Schito, A. Zasso, Characterization of the unsteady aerodynamic response of a floating offshore wind turbine to surge motion, Wind Energy Sci. 5 (4) (2020) 1713–1730, http://dx.doi.org/10.5194/wes-5-1713-2020, URL https://wes.copernicus.org/articles/5/1713/2020/.

[21] S. Cioni, F. Papi, L. Pagamonci, A. Bianchini, N. Ramos-García, G. Pirrung, R. Corniglion, A. Lovera, J. Galván, R. Boisard, et al., On the characteristics of the wake of a wind turbine undergoing large motions caused by a floating structure: an insight based on experiments and multi-fidelity simulations from the OC6 phase III project, Wind Energy Sci. Discuss. 2023 (2023) 1–37.

[22] N. Troldborg, Actuator Line Modeling of Wind Turbine Wakes (Ph.D. thesis), 2009.

[23] A.M. Forsting, N. Troldborg, Generalised grid requirements minimizing the actuator line angle-of-attack error, J. Phys. Conf. Ser. 1618 (5) (2020) 052001, http://dx.doi.org/10.1088/1742-6596/1618/5/052001.

[24] G.P. Navarro Diaz, A.D. Otero, H. Asmuth, J.N. Sørensen, S. Ivanell, Actuator line model using simplified force calculation methods, Wind Energy Sci. 8 (3) (2023) 363–382, http://dx.doi.org/10.5194/wes-8-363-2023, URL https://wes.copernicus.org/articles/8/363/2023/.

[25] L. Martinez, S. Leonardi, M. Churchfield, P. Moriarty, A comparison of actuator disk and actuator line wind turbine models and best practices for their use, in: 50th AIAA Aerospace Sciences Meeting Including the New Horizons Forum and Aerospace Exposition, http://dx.doi.org/10.2514/6.2012-900, arXiv:https://arc.aiaa.org/doi/pdf/10.2514/6.2012-900, URL https://arc.aiaa.org/doi/abs/10.2514/6.2012-900.

[26] H. Rahimi, J. Schepers, W. Shen, N.R. García, M. Schneider, D. Micallef, C.S. Ferreira, E. Jost, L. Klein, I. Herráez, Evaluation of different methods for determining the angle of attack on wind turbine blades with CFD results under axial inflow conditions, Renew. Energy 125 (2018) 866–876, http://dx.doi.org/10.1016/j.renene.2018.03.018.

[27] Atmosphere to Electrons (A2e), OC6 Phase III: Validation of Wind Turbine Aerodynamic Loading During Surge/Pitch Motion, Maintained by A2e Data Archive and Portal for U.S. Department of Energy, Office of Energy Efficiency and Renewable Energy, 2023, https://a2e.energy.gov/ds/oc6/oc6.phase3.